# Validation Assessment of Hypersonic Double-Cone Flow Simulations using Uncertainty Quantification, Sensitivity Analysis, and Validation Metrics

Sarah L. Kieweg*
*Sandia National Laboratories, Albuquerque, NM, 87185-0828*

Jaideep Ray[†]
*Sandia National Laboratories, Livermore, CA,94550-0969*

V. Gregory Weirs[‡], Brian Carnes[§], Derek Dinzl[¶], Brian Freno[‖], Micah Howard[**], Eric Phipps[††], William Rider[‡‡], Thomas Smith[§§]
*Sandia National Laboratories, Albuquerque, NM, 87185*

   **This is the second of three related conference papers focused on verifying and validating a CFD model for laminar hypersonic flows. The first paper deals with the code verification and solution verification activities. In this paper, we investigate whether the model can accurately simulate laminar, hypersonic experiments of flows over double-cones, conducted in CUBRC's LENS-I and LENS-XX wind-tunnels. The approach is to use uncertainty quantification and sensitivity analysis, along with a careful examination of experimental uncertainties, to perform validation assessments. The validation assessments use metrics that probabilistically incorporate both parametric (i.e. freestream input) uncertainty and experimental uncertainty. Further validation assessments compare these uncertainties to iterative and convergence uncertainties described in the first paper in our series of related papers. As other researchers have found, the LENS-XX simulations under-predict experimental heat flux measurements in the laminar, attached region of the fore-cone. This is observed for a deterministic simulation, as well as a probabilistic approach to creating an ensemble of simulations derived from CUBRC-provided estimates of uncertainty for freestream conditions. This paper will conclude with possible reasons that simulations cannot bracket experimental observations, and motivate the third paper in our series, which will further examine these possible explanations. The results in this study emphasize the importance of careful measurement of experimental conditions and uncertainty quantification of validation experiments. This study, along with its sister papers, also demonstrates a process of verification, uncertainty quantification, and quantitative validation activities for building and assessing credibility of computational simulations.**

## Nomenclature

| | | |
|---|---|---|
| $\rho_\infty$ | = | Freestream density |
| $U_\infty$ | = | Freestream velocity |
| $T_\infty$ | = | Freestream temperature |
| $T_{v_\infty}$ | = | Freestream vibrational temperature |

---

*Verification & Validation, Uncertainty Quantification, and Credibility Processes, PO Box 5800, Mail Stop 0828, Albuquerque, NM 87185-0828

[†]Data Science and Analytics, MS 9152, P.O. Box 969, Livermore CA 94550-0969; AIAA Member

[‡]Computational Science, PO Box 5800, Mail Stop 1320, Albuquerque, NM 87185-1320

[§]Verification & Validation, Uncertainty Quantification, and Credibility Processes, PO Box 5800, Mail Stop 0828, Albuquerque, NM 87185-0828

[¶]Aerosciences, PO Box 5800, Mail Stop 0825, Albuquerque, NM 87185-0825

[‖]Verification & Validation, Uncertainty Quantification, and Credibility Processes, PO Box 5800, Mail Stop 0828, Albuquerque, NM 87185-0828

[**]Aerosciences, PO Box 5800, Mail Stop 0825, Albuquerque, NM 87185-0825

[††]Scalable Algorithms, PO Box 5800, Mail Stop 1318, Albuquerque, NM 87185-1318

[‡‡]Computational Science, PO Box 5800, Mail Stop 1320, Albuquerque, NM 87185-1323

[§§]Computational Science, PO Box 5800, Mail Stop 1320, Albuquerque, NM 87185-1320

| | | |
|---|---|---|
| $T_{wall}$ | = | Temperature of the double-cone wall boundary |
| Re | = | Unit Reynolds number |
| $h_{0_\infty}$ | = | Total enthalpy |
| $M_\infty$ | = | Mach number |
| $P_{\text{Pitot}}$ | = | Pitot pressure |

# I. Introduction

THIS conference paper is part of a series of three related papers (the others being [1, 2]) on the verification, validation, and uncertainty quantification (VVUQ) of the Sandia Parallel Aerodynamics and Reentry Code (SPARC). SPARC is a second-order finite-volume simulator, which is being designed for hypersonic CFD simulations on next-generation platforms. These papers aim to establish a body of evidence regarding the capabilities and accuracy of the simulator. This study, with its sister papers, also demonstrates a process of verification, uncertainty quantification, and quantitative validation activities for building and assessing credibility of computational simulations.

SPARC solves the unsteady compressible Navier–Stokes equations for a multi-component reacting mixture of gases, which may be in thermal non-equilibrium. It adopts a finite-volume spatial discretization and the solution is advanced in time using a second-order backward-difference formula. The first paper in this series, Ref. [1], addresses code and solution verification. That paper addresses the numerical solution technique: whether the discrete form of the partial differential equations (PDEs) are solved correctly, and estimates the numerical error. Issues of convergence (under spatial- and temporal-refinement), tolerances on iterative convergence, etc. are also addressed. In this paper, we consider *validation*, i.e., "the process of determining the degree to which a model is an accurate representation of the real world from the perspective of the intended uses of the model." [3]. We do so by simulating experiments and comparing experimental measurements against SPARC predictions. This paper will cover uncertainty quantification (UQ), sensitivity analysis, and validation for a hypersonic, laminar flow over a double-cone. It will include an aggregation of experimental, parametric, iterative and numerical, and experiment–simulation bias uncertainties. Validation metrics are used in the validation assessment.

The experiments in question consist of $M_\infty \approx 12$ flows over a 25º/55º double-cone, which were conducted in the Calspan-University at Buffalo Research Center (CUBRC) Large Energy National Shock Tunnel (LENS-XX) [4] with air as the working fluid. LENS-XX is an *expansion* tunnel. Reference [5] provides a good summary and images of these experiments, such as model dimensions and sensor locations, the key flow features, and the physics models necessary to accurately simulate the flow. The stagnation enthalpies in these experiments vary between 5 MJ/kg and 21 MJ/kg, which produce flows ranging from vibrational non-equilibrium (downstream of the shock structure around the double-cone) to nearly complete dissociation at the highest enthalpies. We chose two extreme cases, Case 1 and Case 4, as listed in Table 2. The 25º cone (henceforth, the "fore-cone"), joins the frustum of a 55º cone (the "aft-cone"), and the instrumentation is heaviest near the frustum to capture the separation bubble and the effects of the shock interaction that the corner induces. The experimental observables consist of pressure and heat-flux measurements at a set of sensors distributed over the entire double-cone.

There have been previous attempts to simulate these experiments [5, 6], including a "blind" code comparison [7]. Ref. [5] provides a good description and plots of the shock-wave/laminar boundary layer interaction on the double-cone. The 25º fore-cone results in an attached shock, whereas the 55º aft-cone results in a detached bow shock. The two shocks, attached and bow, intersect, creating a triple point and a transmitted shock that impinges at a point on the aft-cone. The adverse pressure gradient created by the transmitted shock feeds upstream via the (subsonic) boundary layer, causing the laminar flow to separate upstream of the impingement point. This separated region, in turn, induces a separation shock, which intersects with and modifies the transmitted shock. Plots of these complex shock interactions, and the vortex sheets they induce, can be found in Figure 1, as well as in Ref. [5].

CFD simulations in Ref. [5], where both perfect-gas and non-equilibrium flow models were used, show that the fore-cone pressure is simulated accurately (i.e., it matches LENS-XX measurements), but separation occurs too late. The simulated heat flux under-predicts the measurements significantly, even when measurement errors are taken into account. The authors in Ref. [6] examined whether a more sophisticated model for the coupling between vibrational non-equilibrium and dissociation could explain the mismatch between CFD and experiments. They found that Parks's simple model [8] provided results that were very similar to their more sophisticated one [9]. Furthermore, they found the same under-prediction of heat flux and separation bubble as seen in Ref. [5], as well as accurate CFD predictions for pressure on the fore-cone.

The blind code comparison referred to in Ref. [7] is quite revealing as it shows five different CFD codes failing
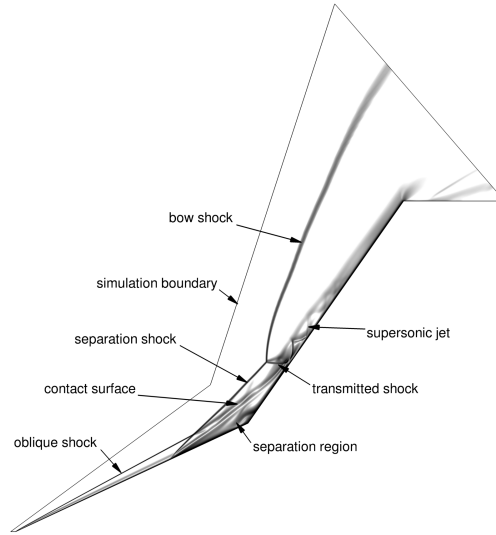
**Fig. 1   This figure shows a simulated Schlieren image of the flowfield from a SPARC simulation of LENS-I Run 35. Simulated Schlieren images essentially show high density gradients, so shockwaves and contact surfaces appear as dark lines.**

to agree with the LENS-XX measurements. In addition, they fail to agree with themselves, despite the fact that their constituent models were similar. The simulation results were grid converged, so the discrepancies were attributed to differences in the grids used by the participants of the blind code comparison exercise. Again, all the models under-predicted the separation zone, mostly due to a delay in predicting the separation bubble, and under-predicted the heat flux.

These difficulties with simulating LENS-XX data parallel those experienced with double-cone experiments in the LENS-I *shock* tunnel [10] in 2000. Navier–Stokes simulations over-predicted the heat flux on the double-cone, though the pressure profile and the separation zone were well predicted [11]. Note that only one experiment, called Run 35, was simulated. However, it was later found that the extreme conditions in the shock tunnel lead to an inflow into the test section that was in strong vibrational non-equilibrium [12]. When the inflow was adjusted accordingly, CFD simulations matched the experimental data quite well. Table 1 lists the original and corrected freestream conditions for Run 35. Again, as with Ref. [6] and LENS-XX, the choice of vibrational non-equilibrium models had little impact on the predictive skill of CFD on LENS-I experiments [13].

In all the studies listed above (i.e., Refs. [5–7]), simulating the experiments implied performing a single simulation, using freestream and other boundary conditions provided by the experimentalists. However, the experimental observables, including the freestream specifications, are uncertain, and these uncertainties have been estimated and provided by the experimentalists. In this paper, we pursue the hypothesis that the uncertainties in the freestream may explain the failure of the previous studies to match experiments, especially if one considers that our quantities of interest (i.e., the pressure and heat fluxes on the test article, as well as the stagnation enthalpies and pressure of the flow upstream of the shock structure) are themselves uncertain.

We will test our hypothesis in the following manner. The freestream uncertainties have been specified by the experimentalists as percentages, not as distributions. Given the constraints imposed by the conservation laws, it is inconceivable that these uncertainties are uncorrelated. However, the correlation structure has not been provided; therefore, we will adopt the maximum-entropy model by (1) using the percentages as the upper and lower bounds of a uniform distribution centered around the nominal values specified in Tables 1 and 2 and (2) assuming that the uniform distributions are independent. We will sample realizations of freestream conditions from this uniform distribution and perform SPARC simulations with them. This ensemble of simulations will provide a distribution of predictions at each of the measurement sensor locations, i.e., at every sensor location, SPARC predictions will take the form of a probability density function (PDF). The uncertain experimental measurements at the same sensors take the form of a uniform PDF. The distance between the prediction and measurement PDFs, as quantified using a Sorensen distance, indicate the degree to which they overlap, and thus how well the simulations reproduce the experimental data.

Note that such a formulation for validating SPARC simulations accomplishes two aims. First, the assumption of maximum entropy distributions is conservative in the sense that it should provide over-dispersed (or overly wide) prediction PDFs. Failure to intersect the measurement PDF is a strong statement regarding the simulation's inability to match experiments. Secondly, ensemble runs allow us to compute the global sensitivity of the quantities of interest (surface pressures and heat flux) with respect to freestream conditions. At the very least, these allow us to identify which freestream uncertainties can be neglected when seeking to explain the prediction-measurement mismatch.

In the following section, we describe the mathematical machinery used to compute sensitivity indices and to perform the ensemble runs. Our strongly probabilistic formulation of the validation problem, relying as it does on global sensitivities and PDFs of predicted and measured quantities, requires an enormous number of freestream realizations ($O(10^4)$) to compute accurately. This is quite intractable due to SPARC's computational cost, if considered naively. Consequently, we will take recourse to ensemble simulations on Smolyak [14] grids defined in the space of freestream conditions, which are then used to construct polynomial chaos expansion [14] surrogates (i.e., statistical emulators of SPARC). Sampling-based statistics and PDFs are computed using these emulators. The complex workflow that underlies these statistical computations is automated using Dakota [15].

## II. Approach

### A. SPARC

SPARC solves the conservation laws for mass, momentum, and energy, formulated for reacting fluids, modeled as continua, where energy in vibrational and translational/rotational modes may not be in equilibrium, i.e., it tracks the two modes using separate conservation laws. The equilibration of vibrational energy is governed by the Landau–Teller model [16], with relaxation time-scales computed using the Millikan–White expression [17]. SPARC can accommodate reacting flows with multiple species, though the simulations in this paper used a 5-species, 17-reaction chemical mechanism for air [18]. In the case of non-equilibrium flows with $T \neq T_v$ (corresponding to the different modes into which energy is partitioned), an effective temperature $T_{\text{eff}} = \sqrt{TT_v}$ is used to compute the chemical reaction rates. Diffusion of individual species is modeled using Lewis numbers, and viscosities for the species are obtained using Blottner's model [19]. Thermal conductivities for the individual species are obtained from Eucken's relations [16], which are then assembled into the mixture's value using Wilke's model [20]. The equations are solved using a finite-volume method with the conserved variables. SPARC accommodates structured and unstructured meshes, though only the former are used in this paper. For the simulations in this paper, we use a Steger–Warming scheme for the inviscid fluxes, extended to second-order accuracy using MUSCL reconstruction. A minmod limiter is used in our simulations. Central differencing is used for diffusion and viscous terms. SPARC solves the unsteady form of the conservation equation, using a three-point backward-difference scheme to achieve second-order accuracy in time. However, all the simulations used in this paper are steady, and the time-integrator is run in its first-order form to accelerate convergence to a steady-state solution.

For all simulations in this paper, we assume the flow over the double-cone is axisymmetric and that the inflow is spatially uniform. No-slip boundary conditions are imposed on the double-cone surface, which is modeled as non-catalytic and is held at a constant temperature of 300 K. These flows are simulated on a stretched mesh. The simulations are run to steady state by reducing the residual by 6 orders of magnitude or by ensuring that 100 flow-through times have been simulated.

### B. Verification & Validation Approach

This is the second of three related papers focused on verifying and validating SPARC for hypersonic, laminar flows. The first paper focuses on code- and solution verification activities [1]. In this paper, we investigate whether the model can accurately simulate hypersonic, laminar flows over double-cones, conducted in CUBRC's LENS-I and LENS-XX wind-tunnels. The third paper [2] examines possible causes for a mismatch between the experiments and simulations, particularly in the laminar, attached flow region on the fore-cone. The following sections present the techniques and results that contribute to the double-cone validation assessment. We examine the available validation experiments and their limitations. The methods for uncertainty quantification and sensitivity analysis, as well as the validation metrics, are described. In concert, these activities are conducted to determine the ability of the models in SPARC to predict the experimental measurements and to ultimately build credibility for hypersonic reentry simulations.

**Table 1    Freestream and boundary conditions for LENS-I experiments. 100% Nitrogen.**

| Experiment | $\rho_\infty$ [kg/m$^3$] | $U_\infty$ [m/s] | $T_\infty$ [K] | $T_{v_\infty}$ [K] | $T_{\text{wall}}$ [K] |
|---|---|---|---|---|---|
| LENS-I, Run 35 (CUBRC nominal) [11, 21, 22] | $5.515 \times 10^{-4}$ | 2713 | 138.9 | 138.9 | 296.1 |
| LENS-I, Run 35 (non-equilibrium) [12] | $5.848 \times 10^{-4}$ | 2545 | 98.27 | 2562 | 296.1 |
| LENS-I, Run 42 (non-equilibrium) [13] | $1.468 \times 10^{-3}$ | 3849 | 268.7 | 2947 | 294.7 |

**Table 2    Freestream conditions for LENS-XX experiments. 76.5% Nitrogen and 23.5% Oxygen. The wall surface temperature, $T_{\text{wall}}$, is assumed to be 300 K [4]. This paper will focus on the lowest and highest enthalpy cases, Case 1 and Case 4.**

| Experiment | $\rho_\infty$ [kg/m$^3$] | $U_\infty$ [m/s] | $T_\infty$ [K] | $T_{v_\infty}$ [K] | Re [m$^{-1}$] | $h_{0_\infty}$ [MJ/kg] | $M_\infty$ | $P_{\text{Pitot}}$ [kPa] |
|---|---|---|---|---|---|---|---|---|
| LENS-XX, Case 1 | $4.999 \times 10^{-4}$ | 3246 | 175 | 175 | $0.14 \times 10^6$ | 5.44 | 12.2 | 5.1 |
| LENS-XX, Case 2 | $9.84 \times 10^{-4}$ | 4303 | 389 | 389 | $0.19 \times 10^6$ | 9.65. | 10.90 | 17.5 |
| LENS-XX, Case 3 | $5.10 \times 10^{-4}$ | 6028 | 521 | 521 | $0.11 \times 10^6$ | 18.70 | 13.23 | 18.0 |
| LENS-XX, Case 4 | $9.640 \times 10^{-4}$ | 6497 | 652 | 652 | $0.20 \times 10^6$ | 21.77 | 12.82 | 39.5 |
| LENS-XX, Case 5 | $1.057 \times 10^{-3}$ | 5996 | 523 | 523 | $0.23 \times 10^6$ | 18.51 | 13.14 | 36.8 |
| LENS-XX, Case 6 | $2.045 \times 10^{-3}$ | 5466 | 573 | 573 | $0.39 \times 10^6$ | 15.23 | 11.46 | 59.0 |

## C. Available Validation Data

The 25º/55º double-cone was subjected to hypersonic conditions in CUBRC's LENS Tunnels. A set of experiments were performed in 2001 in the LENS-I tunnel [11, 21]. These experiments are laminar flows of single species (N$_2$) in mild thermochemical non-equilibrium. In 2014, a new set of experiments over a range of higher total enthalpies was conducted in the LENS-XX tunnel [4]. The LENS-XX experiments are laminar flows of an air mixture in mild to strong thermochemical non-equilibrium in the region downstream of the leading shock. The double-cone was instrumented on the surface for heat flux and pressure measurements on the fore-cone, in the separation region, and along the aft-cone.

Table 1 lists the freestream conditions for the LENS-I experiments referenced in this validation study. CUBRC provided freestream conditions that assumed thermal equilibrium in the freestream. Druguet *et al.* examined the effects of numerical settings, particularly focusing on Run 35 from LENS-I, using the CUBRC-provided freestream conditions shown in the first row of Table 1 [22]. However, Nompelis *et al.* simulated the nozzle and corrected the non-equilibrium freestream conditions in the LENS-I experiment of Run 35 [12]. Run 42 is a higher-enthalpy flow in LENS-I; the computed non-equilibrium freestream conditions were provided in Ref. [13].

Table 2 provides the freestream conditions for the six LENS-XX experiments; Case 1 and Case 4 were chosen for this validation study. The LENS-XX experiments spanned a range of enthalpies higher than those in LENS-I. Case 1 and 4 were chosen for this validation study because they had the smallest and largest enthalpies of the LENS-XX experiments. As for LENS-I, CUBRC assumed thermal equilibrium (i.e., $T_\infty = T_{v_\infty}$) in the freestream. However, as with LENS-I, there are unresolved questions about the freestream conditions in LENS-XX. Two published studies have shown simulations that under-predict the experimental heat flux measurements in the laminar, attached region on the fore-cone when using the CUBRC-provided freestream conditions [5, 6]. The validation study described in this paper will describe our similar results using SPARC, and introduce possible reasons for the computational under-prediction of the laminar, attached region. A companion paper [2] further explores the possible causes for the computational under-prediction of the laminar, attached region and presents an estimation of the inflow parameters and uncertainties.

## D. Experimental Uncertainty Quantification

CUBRC provided a percent error on their assumed thermal equilibrium freestream conditions: $\rho_\infty$: 7%, $U_\infty$: 3%, $T_\infty$: 3% . Their estimation of percentage error includes conservative bounds and subjectivity in their estimates. Consequently, we have assumed uniform distributions (±%) for each input parameter. Because CUBRC assumed thermal equilibrium ($T_{v_\infty} = T_\infty$) in the freestream, they did not state a separate percent error for $T_{v_\infty}$. It is possible to use forward uncertainty quantification studies to explore the effects of independently varying the vibrational temperature, but we do not have an

initial estimate of its uncertainty. The results of our sensitivity analysis and forward uncertainty quantification studies will be themselves sensitive to these assumed input uncertainties.

The uncertainty of the experimentally measured quantities of interest (QoIs) are also a key component for making validation assessments and computing validation metrics. Here, both experimentally and computationally, we are interested in the surface pressure ($p(x)$) and heat flux ($q(x)$) along the length of the double-cone geometry. CUBRC provided heat flux and pressure measurements along the surface of the double-cone at discrete probe locations. They provided a conservative estimate of percent error for these measurements, which we assume and interpret as bounds of a uniform distribution. For LENS-I, CUBRC estimated the the heat flux- and pressure-measurement uncertainties were ± 5% and ± 3%, respectively. For LENS-XX, CUBRC provided error estimates for heat flux and pressure of ± 7% and ± 5%, respectively.

### E. Uncertainty Quantification: Parametric (Input) Uncertainty

*1. Propagation of Freestream Uncertainty*

The goal of a generic uncertaintypropagation problem is to characterize the uncertainty of a model output QoI, given a set of input parameters with characterized uncertainties. Many different approaches are possible. These depend on the number and characterization of the input parameters; the nature of the model, such as whether the model provides just the output quantity or additional information (i.e., derivative information with respect to the input parameters); and the expense associated with evaluating the model. In this section, the approach for estimating the uncertainty of the QoIs ($p(x)$ and $q(x)$) due to the uncertainty of the freestream conditions is described. In this case, the "model" in the uncertaintypropagation problem is comprised of all the physics models (governing equations, boundary and initial conditions, and material models) and numerical approximations necessary for solving those governing equations as instantiated in SPARC. Since uncertainty propagation is used to estimate output uncertainty, it is also called uncertainty quantification (UQ).

Whereas the objective of validation is assessing the physics models, solution verification is used to estimate the numerical error on the grids used for the simulations. Ideally, numerical error can be neglected compared to parametric uncertainty and physics model error. This paper will present that comparison, using solution verification results from our companion paper [1].

The uncertain input parameters are the freestream density ($\rho_\infty$), streamwise velocity ($U_\infty$), temperature ($T_\infty$), and vibrational temperature ($T_{v_\infty}$), which are boundary conditions for the governing equations solved by SPARC. Depending on the type of analysis, we may choose to constrain $T_{v_\infty} = T_\infty$ when assuming thermal equilibrium in the freestream, or allow the two temperatures to vary independently. The information for characterizing them was provided by CUBRC in the form of percentage error, and they were upfront in acknowledging a desire for conservative bounds and the subjectivity in their estimates. Consequently, uniform distributions have been assumed for each input parameter. The stagnation enthalpy and the Pitot pressure are also measured for each CUBRC experiment, and, from a deterministic view, should constrain the freestream parameters to lie in a two-dimensional input parameter space rather than a four-dimensional space. However, the stagnation enthalpy and Pitot pressure are also subject to measurement error, and constraining the freestream variables to the smaller space might skew or under-represent the output uncertainty. Following the conservatism in the selection of the input-parameter bounds, the freestream conditions were unconstrained by the stagnation enthalpy and static pressure measurements. These choices and their consequences are reviewed in the discussion.

*2. Polynomial Chaos Expansions*

The most common "black-box" strategy to estimate output uncertainty is to randomly sample the uncertain input parameters and evaluate the model at the sample points; doing so produces a histogram of the output uncertainty for each of the QoIs. As the number of sample points is increased, the histogram converges to a probability distribution (probability density function (PDF)). The advantages of random-sampling approaches, such as Monte Carlo, quasi-Monte Carlo, and Latin Hypercube Sampling (LHS), are that they are simple to implement and understand, and they converge at the same rate, regardless of the number of input variables. The main disadvantage is that the convergence rate is low, so many samples are required to obtain an accurate characterization of the output uncertainty.

Alternatively, stochastic expansion methods use high-order polynomial approximations to construct a functional mapping between the uncertain input parameters and a QoI. When the QoI is a smooth function of the inputs, the convergence rate is much higher, but the number of model evaluations scales poorly with the number of input parameters.

6

In this work, we use polynomial chaos expansions (PCEs), which are based on multidimensional orthogonal polynomials, evaluated on sparse grids, as implemented in DAKOTA [15]. Since we consider only a small number of input parameters, the PCE approach is much more efficient than sampling.

### 3. Limitations of UQ Approach

Since the input uncertainties are not well characterized and the output uncertainties are functions of the input uncertainties, the output uncertainty results should not be interpreted as precise. The freestream conditions in the double-cone experiments are assumed to be spatially uniform. For Run 35, there is modeling and experimental justification for this assumption, but this does not extend to all LENS-I runs, and there is no evidence for or against spatial uniformity for the LENS-XX cases. In this work, we have focused on *input* parametric uncertainty (i.e., uncertainty of the QoI due to uncertainty of freestream conditions), and not on the uncertainty associated with the numerical settings.

## F. Sensitivity Analysis

In sensitivity analysis, one tries to determine which input parameters have the largest influence over a QoI. Results will be presented in this paper for both local- and global-sensitivity analysis. SPARC supports a form of forward-embedded local-sensitivity analysis where local partial derivatives of response quantities of interest with respect to model parameters and boundary conditions are computed internally within SPARC. Local sensitivity, for the purposes of this paper, is defined as follows. Let $\phi_i$ be a QoI, e.g., pressure at a location $i$. Let $p_j$ be the $j^{\text{th}}$ parameter being perturbed. Then, sensitivity $s_{ij}$ is described as

$$s_{ij} = \frac{p_j}{\phi_i} \frac{\partial \phi_i}{\partial p_j}.$$

The discrete nonlinear equations implemented in SPARC are differentiated using the Sacado automatic differentiation package, resulting in a new set of sensitivity equations that are then solved along side the original equations using pseudo-transient time integration [23–26]. This allows local sensitivities with respect to a small number of parameters to be computed accurately and efficiently without finite-difference truncation error and only requires a few additional lines in the SPARC input file. This method was employed to screen out potentially insignificant parameters for subsequent uncertainty propagation and calibration calculations, and to efficiently assess sensitivity prior to conducting a global sensitivity analysis.

In contrast, global sensitivity analysis integrates the effects of each parameter over the input parameter space as the basis for estimating influence. As for uncertainty propagation, the input parameters must be characterized, and the global sensitivity analysis results critically depend on this characterization. In fact, many of the methods used for uncertainty propagation are also used for global sensitivity analysis, and, in some cases, the only distinction is in the interpretation of the results.

In this work, Sobol' sensitivity indices are used to measure input-variable sensitivities; the variance of the QoI across all of the inputs is computed and then apportioned to each of the input parameters. The "main effects" index, $S_i$, measures the influence of parameter $i$ alone, and the "total effects" index, $S_{Ti}$, measures the influence of the parameter and all its interactions. Index values near zero indicate that the QoI is insensitive to parameter $i$. The sum of the main effects indices, $\sum_i S_i$, is less than or equal to unity, and $S_i \approx 1$ indicates that parameter $i$ dominates the effects of the others. The sum of the total effects indices is greater than or equal to unity, but values can be interpreted in the same way as for the main effects indices.

Because PCE provides a functional mapping between the input parameters and QoI, the Sobol' sensitivity indices can be evaluated analytically. They can also be estimated when random sampling approaches are used, but they require many more function evaluations and provide only approximate results. (In most uses of sensitivity analysis, approximate results are sufficient.)

## G. Validation Metrics

The simplest and least-informative validation assessment is a straightforward scalar metric of the difference (or bias) between a deterministic simulation result and the corresponding nominal experimental measurement at each probe location. However, the uncertainty propagation activities described above will yield a distribution of computational predictions at each measurement location along the length of the cone, i.e., at each sensor location. This distribution represents one major element of parametric uncertainty — the input uncertainty due to uncertain freestream conditions.

These SPARC predictions can be represented and visualized as a PDF. At each sensor location, the uncertain experimental measurements are assumed in the form of a uniform PDF.

For a qualitative validation assessment, one can visually compare the distance and/or overlap between the prediction PDF and the observation PDF, examining the difference at each measurement probe location. However, it is beneficial to have quantitative, objective measures of predictive accuracy. In addition, a comparison using only parametric uncertainty (of the prediction) and the experimental uncertainty does not consider other sources of uncertainty. In particular, we are interested in how the experimental and parametric uncertainties compare to uncertainties quantified in the solution verification activities: numerical uncertainty (i.e., from mesh convergence studies) and iterative uncertainty. Other sources of uncertainty can include analyst-to-analyst variability (e.g., different grids), surrogate error from the PCE process in the uncertainty propagation activity, other parametric uncertainties (e.g., from the chemistry or viscosity models), and other numerical uncertainties from other numerical settings. The example of analyst-to-analyst variability based on different grid design will be briefly examined, but these other sources will not be considered quantitatively in this study.

As part of the evaluation of freestream conditions $\Theta$, we will have to compare its predictions $\mathbf{z}$, as generated by SPARC, with observations $\mathbf{z}_{\mathrm{obs}}$. Here $\mathbf{z} = \{z_j\}, j = 1 \ldots J$ is a vector of predictions, e.g., pressures at a set of $J$ probes. If we are provided with a single $\Theta$, we can compute the root-mean-square error (RMSE) between $\mathbf{z}$ and $\mathbf{z}_{\mathrm{obs}}$ to obtain a simple figure of merit for the quality of $\Theta$. However, under an uncertain characterization of freestream conditions, we have a PDF $P(\Theta)$, which does not lend itself to a single figure of merit using RMSE. More accurately, our observations $\mathbf{z}_{\mathrm{obs}}$ are also uncertain (measurement errors are specified using percentages); therefore, we model the uncertain observations as a uniform distribution $Q(\mathbf{z}_{\mathrm{obs}})$, with the bounds computed using the error percentages. For convenience, we also require a single figure of merit to compare the quality of $P(\Theta)$ given $Q(\mathbf{z}_{\mathrm{obs}})$.

Therefore, in order to compare the SPARC predictions to the experimental observations for each experimental case, we will use the following validation assessments.

*1. Validation Metrics for Certain Observations*

For comparison of *uncertain* predictions with a *certain* representation of observations, we use a scalar metric, a Continuous Ranked Probability Score (CRPS, [27, 28]), as a function of spatial location on the cone, CRPS($x$). We will use the CRPS as the figure of merit for $P(\Theta)$ given $\mathbf{z}_{\mathrm{obs}}$ (note, *not* $Q(\mathbf{z}_{\mathrm{obs}})$). The CRPS is computed for each probe, and a single figure of merit obtained by taking the average over all $J$ probes. We take a set of $\Theta$ samples, $\Theta^{(m)}, m = 1 \ldots M$, and compute predictions $\mathbf{z}^{(m)}$. Thus, at every probe $j$, we have the predictions $z_j^{(m)}$, which allow us to construct a predicted distribution $Q'(z_j)$ to be compared with $z_{obs,j}$. Let $Q'_{c,j}(z)$ be the cumulative distribution function (CDF) corresponding to the probability density $Q'(z_j)$. The CDF of the perfect observation $z_{obs,j}$ is the Heaviside function $\mathbb{H}(z_{obs,j})$. The CRPS of the prediction at the $j^{\mathrm{th}}$ probe, $\mathrm{CRPS}_j$, is defined as

$$\mathrm{CRPS}_j = \int_{\infty}^{\infty} \left( Q'_{c,j}(y) - \mathbb{H}(y - z_{\mathrm{obs},j}) \right)^2 dy. \tag{1}$$

Thus $\mathrm{CRPS}_j$ has units of the observed quantity $z_{\mathrm{obs},j}$. Small values of $\mathrm{CRPS}_j$ denote a good match between predictions and observations. We will denote the mean of $\mathrm{CRPS}_j$ as CRPS.

*2. Validation Metrics for Uncertain Observations*

CRPS, as defined above, will be used to gauge the quality of $P(\Theta)$ when we are not quite sure of our uniform-distribution model for $Q(\mathbf{z}_{\mathrm{obs}})$. For consideration of *uncertain* experimental observations, we assume the uniform-distribution model for measurement errors and gauge the quality of $P(\Theta)$ using the Sorensen distance $d_S$ [29]. The Sorensen distance quantifies the distance between the prediction and measurement PDFs and indicates the degree to which they overlap.

Let $Q(y)$ denote the PDF of the observed quantity $z_{\mathrm{obs},j}$. Let $Q'(y)$ be the PDF of the predicted quantity $z_j$ at probe $j$. Let $Q_k(y)$ and $Q'_j(y)$ be their discretized form on a 1-D discretization of the $y-$space. Then, $d_S$ between $Q(y)$ and $Q'(y)$ is defined as

$$d_S = \frac{\sum_k |Q_k - Q'_k|}{\sum_k (Q_k + Q'_k)}. \tag{2}$$

$d_S = 0$ indicates a perfect match. $d_S = 1$ corresponds to $Q(y)$ and $Q'(y)$ being disjoint.

## 3. Comparison of Uncertainties

Relative errors from several uncertainty sources will be plotted and compared along spatial location for each experiment, and compared to the relative-difference bias between the deterministic simulation and the nominal experimental values. The uncertainty sources will be: parametric uncertainty (from the uncertainty-propagation results), experimental uncertainty (provided by CUBRC), numerical uncertainty (i.e., mesh convergence), and iterative uncertainty. The relative parametric uncertainty, $u_{\text{param, rel}}$ was estimated as follows:

$$u_{\text{param, rel}} = \frac{(\mu + 2\sigma) - (\mu - 2\sigma)}{\mu}, \tag{3}$$

using the mean ($\mu$) simulation and the standard deviation ($\sigma$) from the ensemble of simulations resulting from the uncertainty propagation. In other words, at each location along the cone, it represents approximately 95% of the values that lie within two standard deviations of the mean, and is normalized by the mean simulation result. The relative iterative uncertainty was estimated using the median SPARC prediction compared to a reference solution at high iterations (200,000 for Case 4, 83,000 for Case 1) and the finest mesh ($1024 \times 512$):

$$u_{\text{iter, rel}} = \frac{|\text{median} - \text{reference}|}{\text{median}} \tag{4}$$

The relative numerical uncertainty was estimated using the median SPARC prediction compared to the extrapolated numerical solution:

$$u_{\text{num,rel}} = \frac{|\text{median} - \text{extrapolated}|}{\text{median}} \tag{5}$$

Our companion paper [1] describes the solution verification methods for the reference high-iteration solutions and extrapolated numerical solutions used in the relative numerical and iterative uncertainties. The relative experimental uncertainty ($u_{\text{expt, rel}}$) was determined from CUBRC-provided estimates. For LENS-I, CUBRC estimated the the heat flux- and pressure-measurement uncertainties were ± 5% and ± 3%, respectively. For LENS-XX, CUBRC provided error estimates for heat flux and pressure of ± 7% and ± 5%, respectively.

## 4. ASME V&V20 Validation Metric

The uncertainties examined in the above comparison will be combined into another validation metric, as described in the ASME V&V20 *Standard for Verification and Validation in Computational Fluid Dynamics and Heat Transfer* [30]. The absolute bias, $|E| = |S - D|$, is the difference between the median simulation and the experimental measurement. At each spatial location, an overall validation uncertainty was calculated as follows:

$$u_{\text{val, rel}} = \sqrt{u_{\text{param, rel}}^2 + u_{\text{iter, rel}}^2 + u_{\text{num, rel}}^2 + u_{\text{expt, rel}}^2} \tag{6}$$

$$u_{\text{val}} = (u_{\text{val, rel}})(\text{median}) \tag{7}$$

The median is the median simulation from the uncertainty propagation activity. The results section will show plots of the absolute bias along with uncertainty ranges, as well as $\frac{|E|}{u_{\text{val}}}$.

# III. Results and Discussion

## A. Deterministic Simulations

In this section, we first present example SPARC simulations in a deterministic manner, i.e., with a single set of freestream conditions as input, and without considering uncertainty in those input. In the next sections, we will provide examples of how uncertainty propagation techniques allow us to add parametric uncertainty to the simulation in order to consider uncertainty in the simulation results, as well as in the experimental observations.

Fig. 2 gives an example flowfield around the double-cone geometry. This example is for LENS-XX Case 4, using the freestream conditions listed in Table 2. The plot on the left shows contours of the temperature through the flow field and demonstrates some of the features in the different areas of the cone, which make this simulation challenging and interesting to study. On the fore-cone, there is a laminar, attached shock, which separates near the inflection point to the
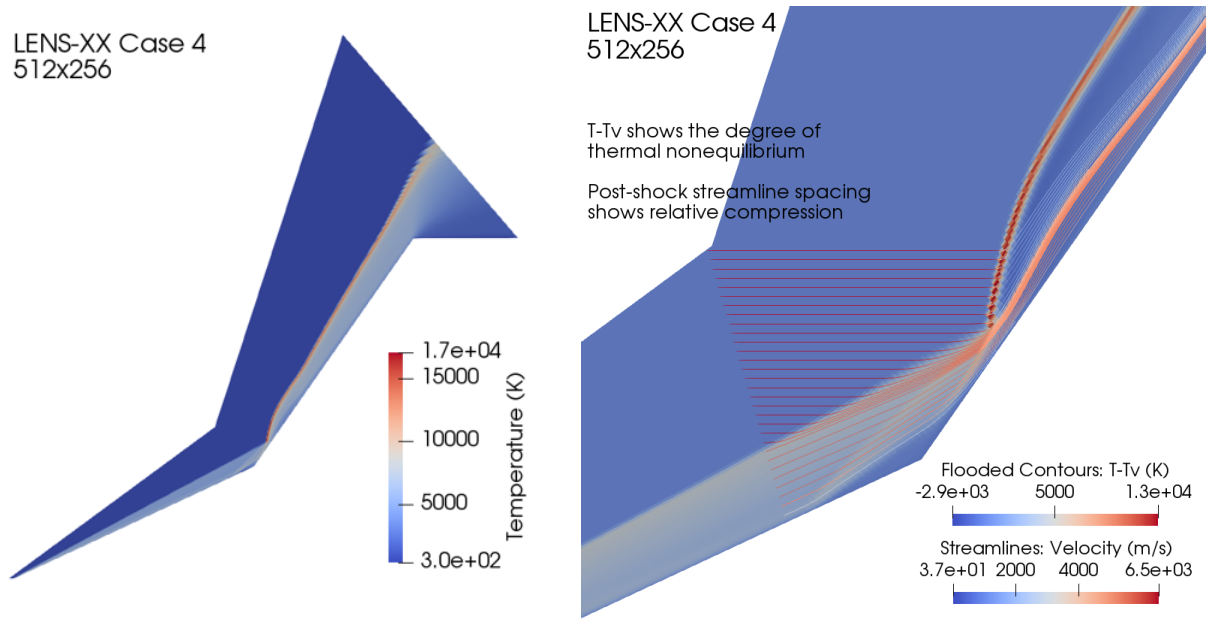
**Fig. 2  Example flowfield around the double-cone geometry using freestream conditions given in Table 2 for LENS-XX Case 4. Mesh size: $512 \times 256$. Left: Flooded contours for the temperature. Right: Flooded contours for the difference between the temperature and vibrational temperature, i.e., $T - T_v$; Streamlines for velocity.**

second cone. The separation shock and region spans the cone corner, where an intersection meets near the surface of the second cone at the transmitted shock and near the impingement point. Near the aft-cone, there is a supersonic jet and a detached shock. (Not all features are visible in this example image).

The plot on the right of Fig. 2 shows flooded contours of the difference between the temperature and vibrational temperature, i.e., $T - T_v$, in the flowfield around the double-cone. This is an interesting measure because it demonstrates the strong thermal non-equilibrium. Immediately behind the shock, $T_v < T$, and then they approach each other as the internal energies (vibrational and translational) equilibrate. In the separation bubble in the corner, $T$ is approximately equal to $T_v$. This is because the gas recirculates in the bubble at a relatively low speed; therefore, it has time to equilibrate. The plot on the right of Fig. 2 also shows streamlines for the velocity. Streamlines clustered together generally indicate compression; streamlines spread apart indicate expansion.

Fig. 3 shows an example of a deterministic simulation by SPARC of LENS-I Run 35. These figures show the heat flux and pressure on the surface of the cone along the length of the cone. The heat flux decreases along the attached region, then drops abruptly in the separated zone. It increases again to a maximum located at the impingement point on the aft-cone. The simulations are plotted alongside the experimental probe measurements, with error bars indicating the CUBRC-provided experimental error estimates. The green curve shows the Run 35 simulations using the original CUBRC-provided freestream conditions, which assumed thermal equilibrium in the freestream. As Druguet *et al.* and Nompelis *et al.* demonstrated, the Run 35 simulations greatly over-predict the heat flux experimental measurements on the fore-cone, in the laminar, attached region [12, 22]. Using the computed non-equilibrium freestream conditions from Nompelis *et al.* (the red curve in Fig. 3), the simulation appears to better predict the experiment in the attached region.

SPARC solutions were compared to solutions generated by colleagues at the University of Minnesota using US3D for LENX-XX Cases 1-6 [7]. US3D is a finite-volume Navier-Stokes solver with finite-rate thermochemistry developed at the University of Minnesota [31]. SPARC solutions compare favorably to solutions using US3D. Figures 4 and 5 show the comparison of SPARC solutions to Minnesota's US3D solutions for Cases 1-6 of LENS-XX. Overall, these are favorable comparisons. Similar to US3D and other CFD codes shown in the blind code comparison referred to in Ref. [7], SPARC under-predicts the heat flux in the attached region as well as under-predicts the separation zone of the six LENS-XX cases, mostly due to a delay in predicting the separation point. The trend is magnified for the higher enthalpy cases where there is stronger thermochemical nonequilibrium. We do observe differences between SPARC and US3D in the separation region and the aft-cone, and these differences increase with larger enthalpy cases. In these
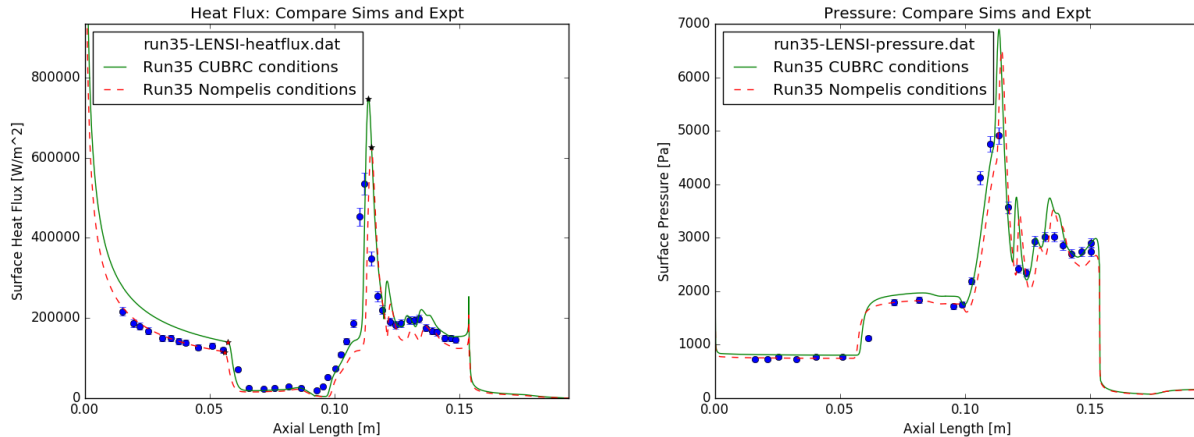
**Fig. 3  SPARC deterministic simulation using freestream conditions for LENS-I Run 35 given in Table 1. SPARC simulations use a 512 × 1024 mesh, 50000 iterations, 5-species, 1-temperature model. Experiment error bars: heat flux, ±5%; pressure, ±3%; per CUBRC. Left: Heat flux distribution along the cone. The small red star on the green curve indicates the approximate detachment point, as detected by a sharp drop in the heat flux in the simulation at the beginning of the separation region. The small black star at the maximum peak of the green curve indicates the approximate impingement point on the second cone, as indicated by the maximum heat flux in the simulation. Right: Pressure along the cone.**

regions, SPARC solutions are still sensitive to mesh and iterative convergence (see our companion paper [1]), and so we may expect to see these differences between SPARC and US3D. We confirmed that SPARC solutions using our own mesh matched SPARC solutions using the Minnesota mesh (both 512 × 1024 resolution for LENS-I Run 35), which suggests the mesh itself is not a source of differences (comparison not shown here). Overall, the differences between SPARC and US3D in the separation region are much smaller than the difference in comparison to the experimental measurements.

### B. Uncertainty Propagation

Figures 6 and 7 demonstrate the parametric uncertainty around a deterministic simulation for LENS-XX Cases 1 and 4. The SPARC deterministic simulation is plotted with the green curve, alongside the blue experimental measurements. On the left, we observe that the deterministic simulation result under-predicts the experimental heat flux measurements in the laminar, attached region of the fore-cone. The under-predictions were observed to various degrees in all six cases of LENS-XX. The under-predictions have also been observed by other researchers in recent publications [5, 6]. Figures 6 and 7 also show an example of using uncertainty propagation techniques to represent parametric (specifically, input) uncertainty. For this ensemble of uncertainty propagation simulations, a level-2 PCE surrogate was built from 31 original SPARC simulations. Then, 10,000 evaluations of the PCE surrogate were used to plot the quantile and median simulation lines. This ensemble was built using 7%, 3%, and 3% uniform uncertainty of $\rho$, $U_\infty$, and $T_\infty$, based on CUBRC-supplied estimates of uncertainty on freestream conditions. In this example, we assume thermal equilibrium in the freestream (as CUBRC assumed) and set $T_{v_\infty} = T_\infty$, so that $T_{v_\infty}$ is always perturbed along with $T_\infty$. This ensemble forms an estimate of the parametric uncertainty, specifically from the freestream input uncertainty. All simulations used a 512 × 1024 mesh at 100,000 iterations determined to be sufficiently converged based on our companion study of solution verification [1].

In this section, we showed that we are unable to bracket the experimental measurements of heat flux for Case 1 and Case 4 in the laminar, attached region and in the aft-cone of Case 4 using CUBRC-provided estimates of freestream uncertainty (see Figs. 6 and 7). However, with ± 15% perturbations, we were able to bracket observations on the fore-cone (not shown here). Our companion paper [2] explores this further in the context of estimating freestream conditions.

As noted in our companion paper [1], the regions around the separation and on the aft-cone are very sensitive to mesh and iterative convergence. In the sections below, this computed parametric uncertainty will be compared with the
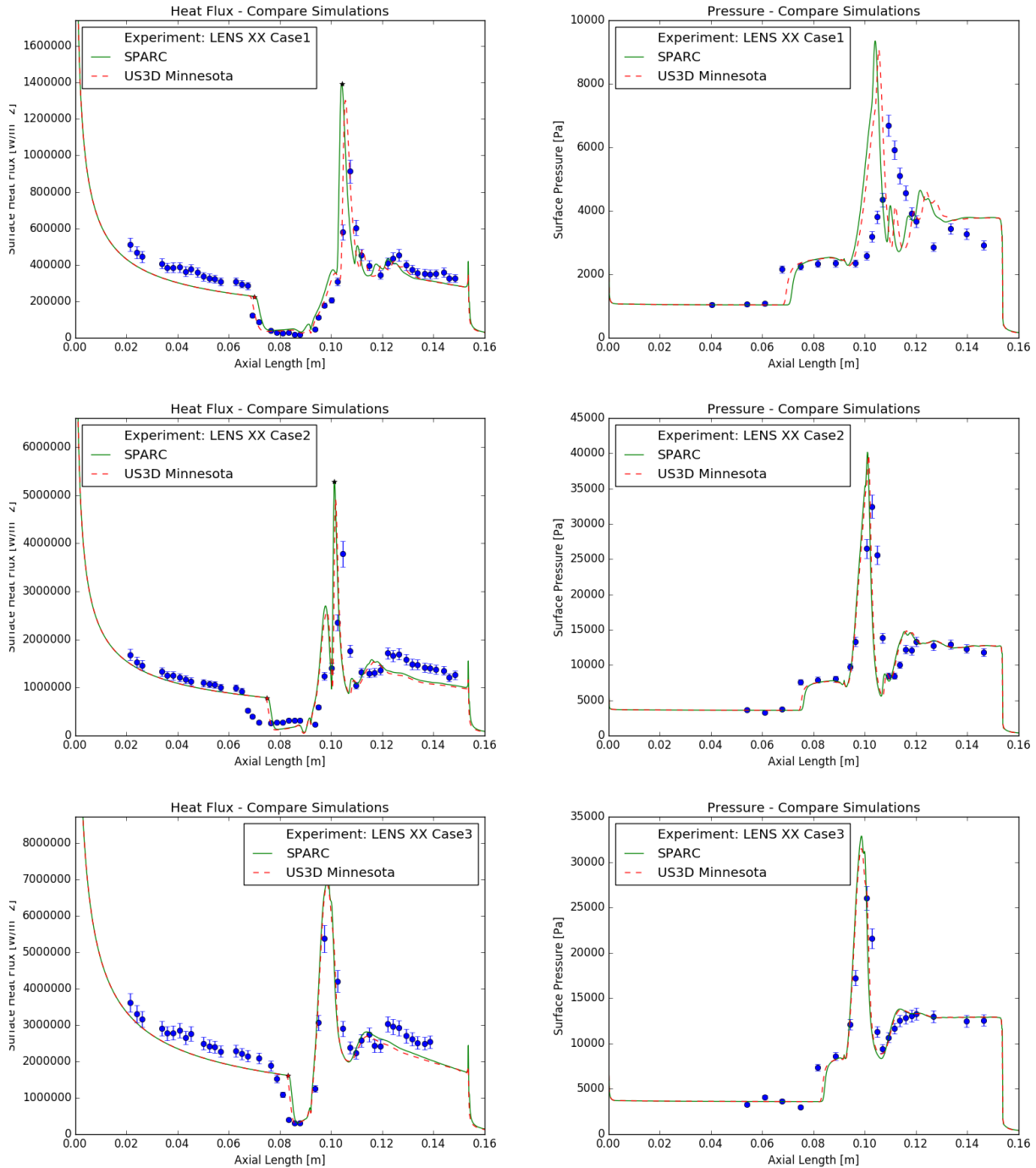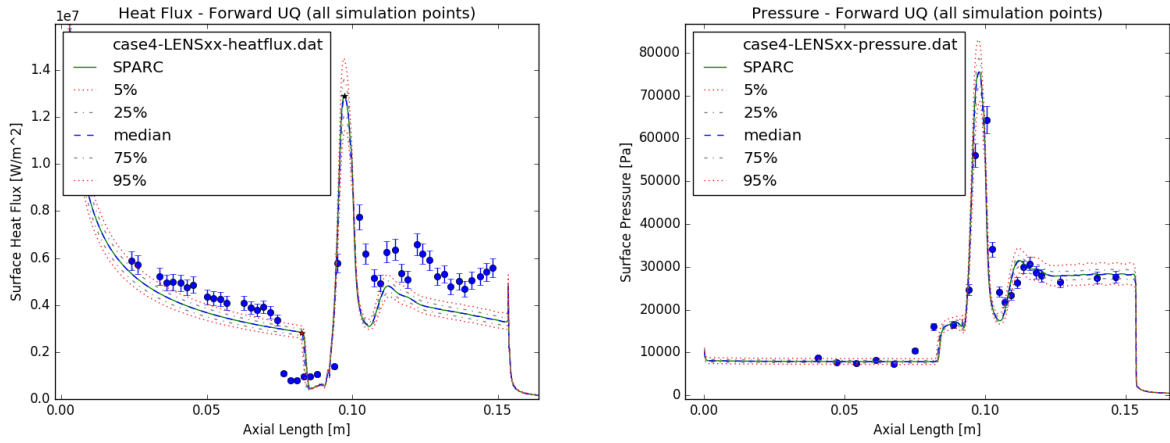
**Fig. 4  LENS-XX Cases 1–3 SPARC solutions shown with experiments and US3D solutions (provided by University of Minnesota). Both US3D and SPARC used 512 × 1024 meshes. SPARC simulations use 100,000 iterations and a 5-species, 2-temperature model. Experiment error bars: heat flux: ±7%, pressure: ±5%, per CUBRC.**
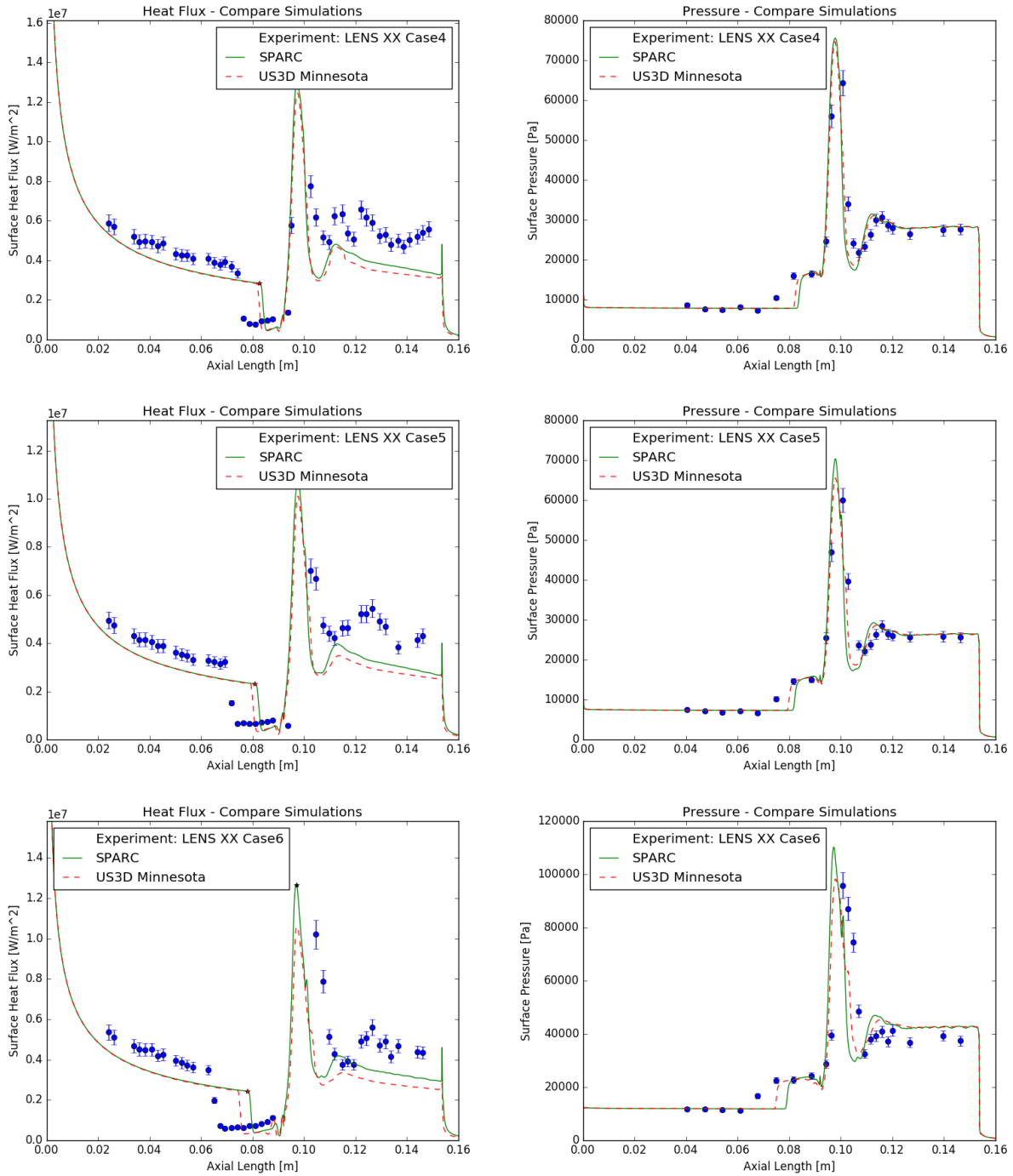
**Fig. 5  LENS-XX Cases 4–6 SPARC solutions shown with experiments and US3D solutions (provided by University of Minnesota).  Both US3D and SPARC used 512 × 1024 meshes.  SPARC simulations use 100,000 iterations and a 5-species, 2-temperature model.  Experiment error bars: heat flux: ±7%, pressure: ±5%, per CUBRC.**
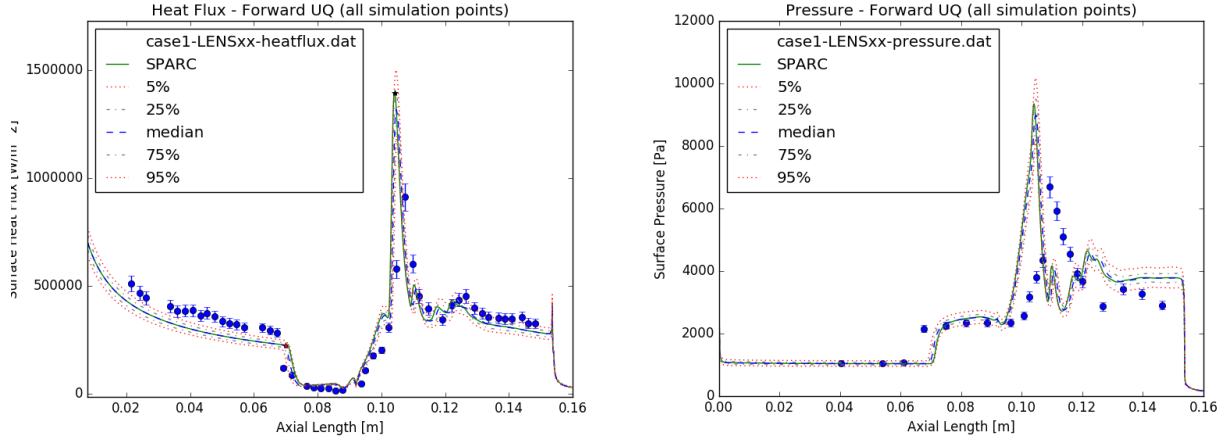
**Fig. 6  LENS-XX, Case 1: Uncertainty propagation along with a deterministic SPARC simulation. SPARC simulations used a 512 × 1024 mesh; 100,000 iterations; and a 5-species, 2-temperature model. Uncertainty propagation ensembles created using 7%, 3%, and 3% uncertainty on $\rho$, $U_\infty$, and $T_\infty$, per CUBRC-supplied uncertainty on freestream conditions. In this example, we assume thermal equilibrium in the freestream and set $T_{v_\infty} = T_\infty$, so that $T_{v_\infty}$ is perturbed along with $T_\infty$. Ensemble of 10,000 evaluations of a PCE surrogate (level 2) built from 31 original SPARC runs. Experimental error bars: heat flux, ±7%, pressure: ±5%, per CUBRC.**



**Fig. 7  LENS-XX, Case 4: Uncertainty propagation along with a deterministic SPARC simulation. SPARC simulations used a 512 × 1024 mesh; 100,000 iterations; and a 5-species, 2-temperature model. Uncertainty propagation ensembles created using 7%, 3%, and 3% uncertainty on $\rho$, $U_\infty$, and $T_\infty$, per CUBRC-supplied uncertainty on freestream conditions. In this example, we assume thermal equilibrium in the freestream and set $T_{v_\infty} = T_\infty$, so that $T_{v_\infty}$ is perturbed along with $T_\infty$. Ensemble of 10,000 evaluations of a PCE surrogate (level 2) built from 31 original SPARC runs. Experimental error bars: heat flux: ±7%, pressure: ±5%, per CUBRC.**

14

convergence and iteration uncertainty (from our companion paper [1]), as well as experimental uncertainty. We have also examined evidence that a level-3 PCE surrogate shows little difference over a level-2 PCE surrogate (not shown here), and we estimate that surrogate error is negligible in comparison to other sources of uncertainty. Finally, this estimate of parametric uncertainty will be used in the validation metrics in later sections.

### C. Sensitivity Analysis

In Fig. 8, we plot the local sensitivities for LENS-XX Case 1 around the nominal conditions. Local sensitivities were generated with SPARC's embedded sensitivity analysis. We see that the heat flux is barely sensitive to perturbations of $T_\infty$ and $T_{v_\infty}$. The sensitivity to $U_\infty$ perturbations is about an order of magnitude larger than that due to $\rho_\infty$. In our companion paper [2], we present global sensitivity analysis results for Case 1 at the probe locations and find that, qualitatively, the sensitivity results agree. This inspires confidence in our calculation of Sobol' indices.

Fig. 9 shows an example of local and global sensitivity analysis of LENS-XX Case 4. In the top figure, the local sensitivity of heat flux to each of the four freestream parameters is plotted along the length of the double-cone (entire length not shown here). As with Case 1 in Fig. 8, the heat flux for Case 4 is most sensitive to freestream velocity, and negligibly sensitive to $T_\infty$ and $T_{v_\infty}$. In the bottom figure, global sensitivity is represented with Sobol' indices for heat flux. As with local sensitivity, we see that the vast majority of variation in heat flux is due to changes in velocity; both temperatures have a minor influence.

Figure 10 shows the results of the global sensitivity analysis along the entire flowfield for both Cases 1 and 4. The global sensitivity is represented with Sobol' indices for heat flux and pressure. As with local sensitivity, we see that the vast majority of variation in heat flux is due to changes in velocity; the temperature has a minor influence. In these studies, we used CUBRC-provided estimates of uncertainty for $\rho$, $U_\infty$, and $T_\infty$, and set $T_{v_\infty} = T_\infty$. Thus, the individual impact of $T_{v_\infty}$ is not computed here, but is expected to be negligible based on the results shown above.

### D. Validation

*1. Validation Metrics for Certain and Uncertain Observations*

As described in the Approach section, for comparison of *uncertain* predictions with a *certain* representation of observations, we use a scalar metric, a Continuous Ranked Probability Score, as a function of spatial location on the cone. Thus, $\text{CRPS}_j$ has units of the observed quantity $z_{\text{obs},j}$. Small values of $\text{CRPS}_j$ denote a good match between predictions and observations. We will denote the mean of $\text{CRPS}_j$ as CRPS. For consideration of *uncertain* experimental observations, we assume the uniform distribution model for measurement errors and gauge the quality of $P(\Theta)$ using the Sorensen distance $d_S$ [29]. $d_S = 0$ indicates a perfect match. $d_S = 1$ corresponds to $Q(y)$ and $Q'(y)$ being disjoint.

Figures 11 and 12 plot these two metrics for Case 1 and Case 4. The metrics are shown for both heat flux and pressure, at each probe location along the length of the cone. These distances were calculated using the ensemble results from the uncertainty propagation studies presented in the previous sections. These metrics will be compared to results after calibration in our companion paper [2]. We see that the CRPS values for pressure are large at the separation point and the region downstream of reattachment, regardless of total enthalpy of the flow. This is paralleled in the plots for the Sorensen distance $d_S$, which saturates at 1.0 (i.e., no overlap between the prediction and measurement PDFs) for large sections of the flow aft of the reattachment point. Matters are worse for the heat flux predictions — $d_S = 1$ everywhere except for the first few probes on the fore-cone. Also, we observe that $d_S$ for the heat flux on the aft-cone is less for Case 1 than for Case 4, where there is a greater mismatch in the heat flux on the aft-cone.

*2. Comparison of Uncertainties*

The top row in Figure 13 shows a comparison of the relative errors in heat flux and pressure for Case 4, derived from several sources of uncertainty: experimental error (using CUBRC-provided uncertainty ranges), two standard deviation range from parametric uncertainty (from the uncertainty propagation studies), iterative errors, and numerical uncertainty.

The relative bias reflects the relative difference between the median SPARC prediction and the experimental observation, normalized by the median SPARC prediction. The relative iterative uncertainty was estimated using the median SPARC prediction compared with a reference solution at high iterations (200,000 for Case 4, 83,000 for Case 1) and the finest mesh ($1024 \times 512$). Similarly, the relative numerical uncertainty was estimated using the extrapolated solutions from solution verification methods in our companion paper [1].
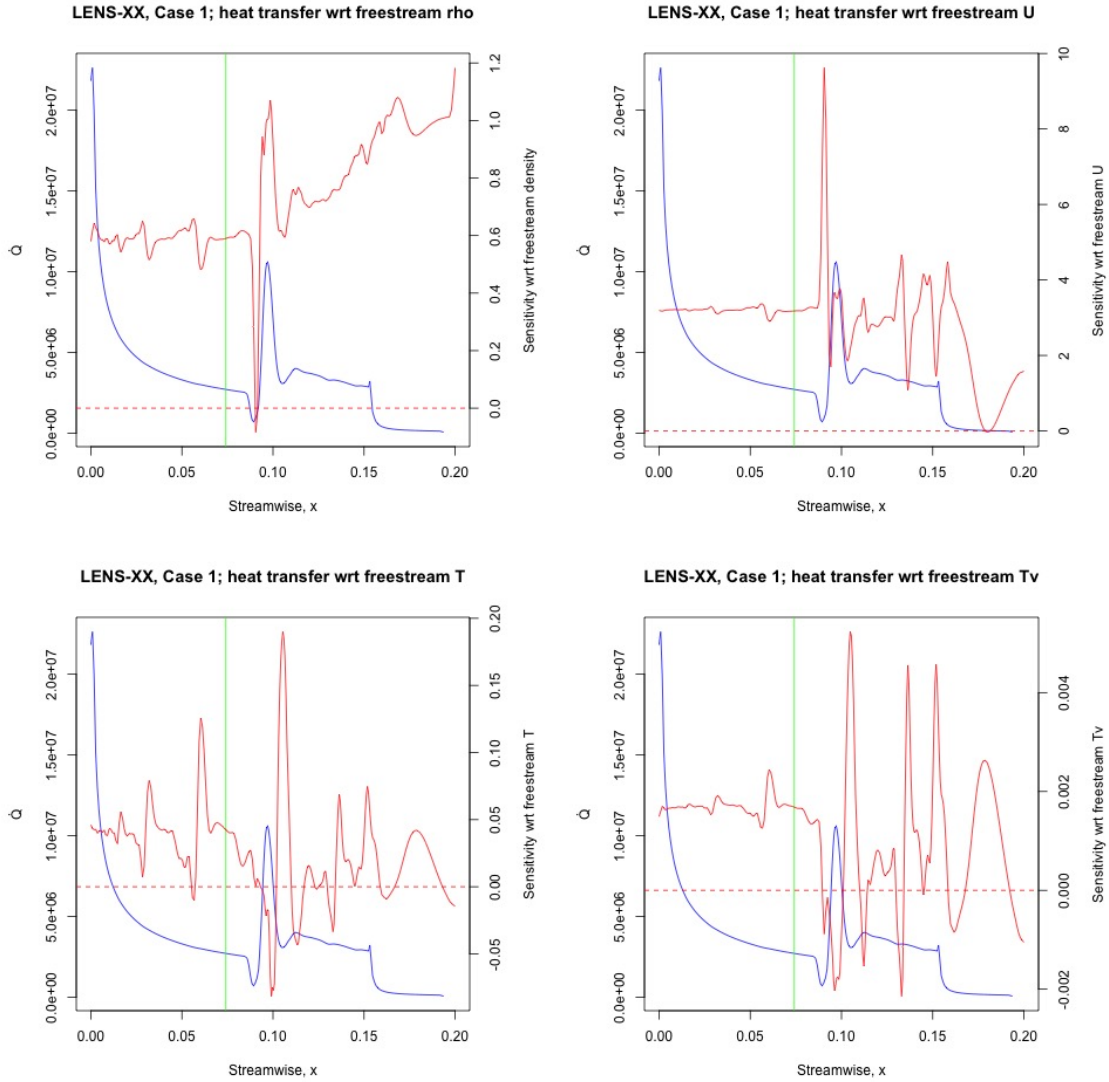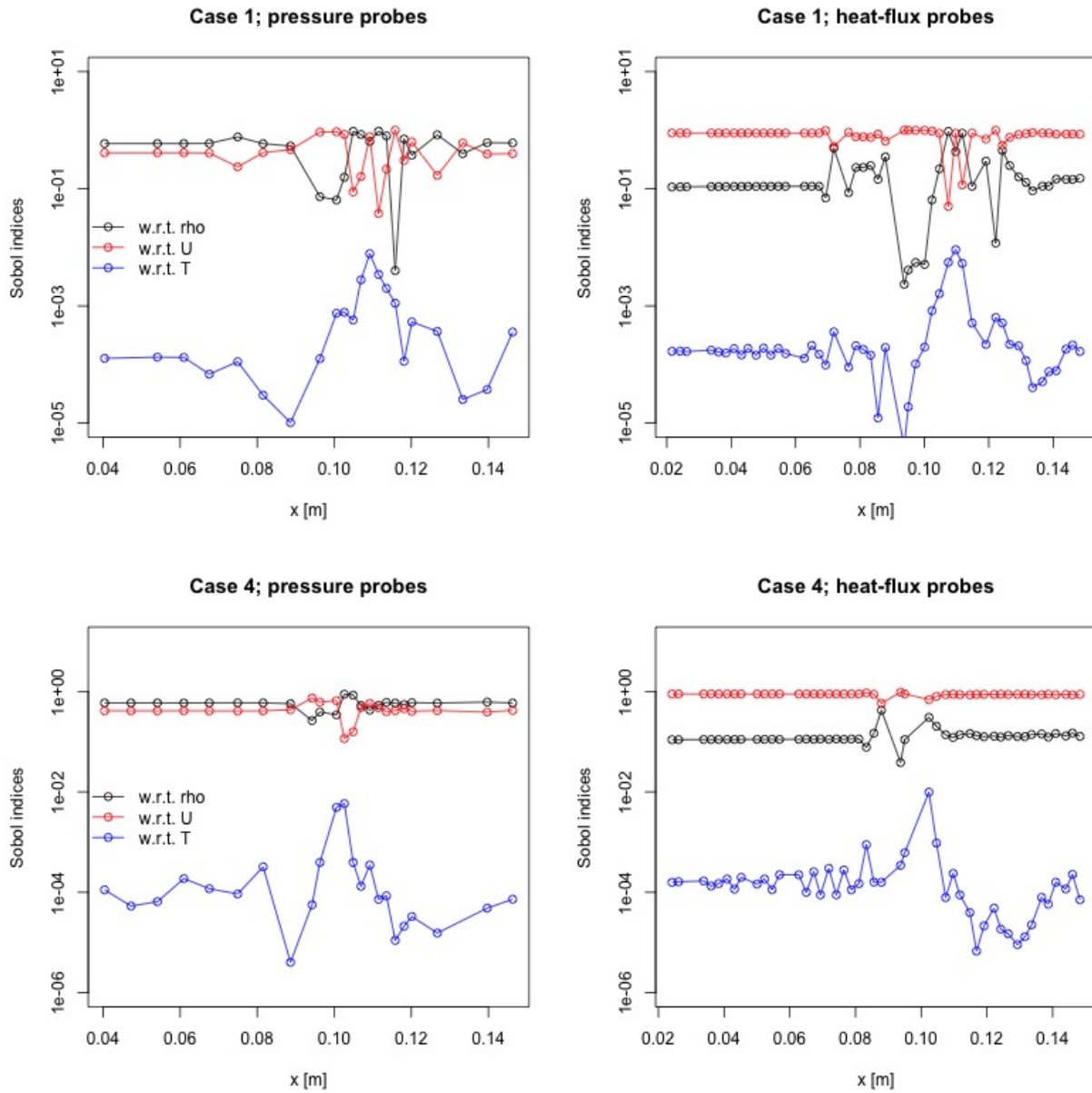
**Fig. 8** Local sensitivities of the heat flux for Case 1 due to perturbation of freestream conditions. Sensitivities for $\rho_\infty$, $U_\infty$, $T_\infty$ and $T_{v_\infty}$ are plotted (top left, top right, bottom left and bottom right). The vertical green line shows the location where the flow becomes detached. The dashed horizontal line denotes zero. The blue line is the heat flux predicted by SPARC using nominal inputs and is plotted for reference.
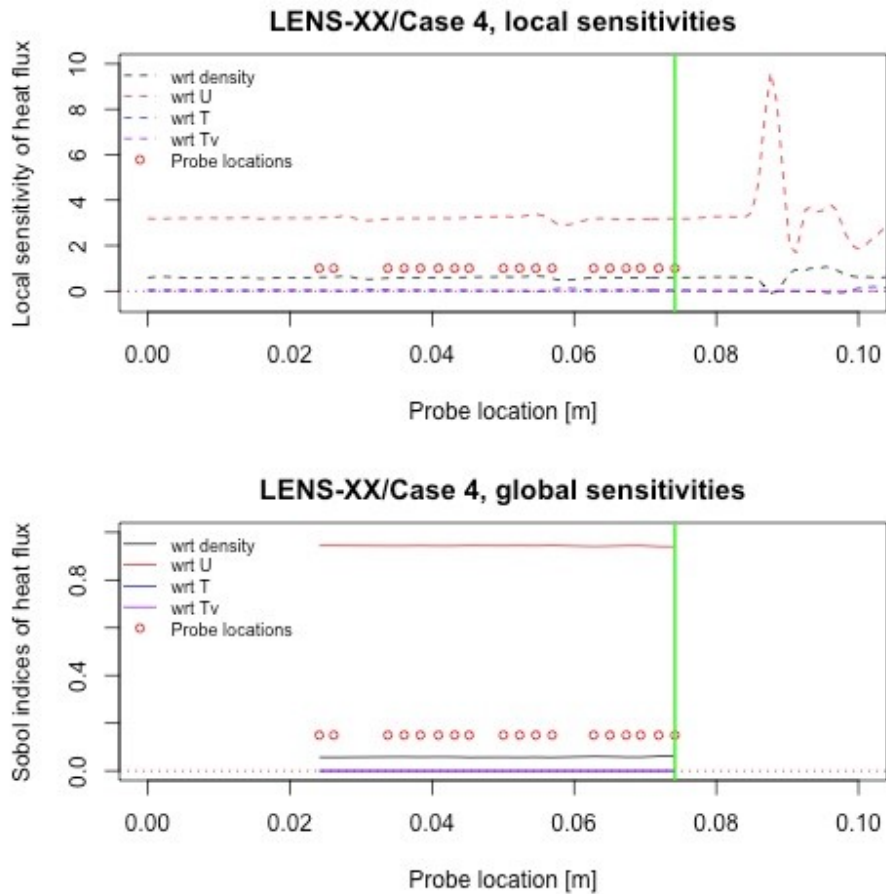
**Fig. 9 Local (top) and Global (bottom) Sensitivity Analysis for LENS-XX Case 4. Heat flux measurements are shown at the experimental probe locations only on the fore-cone. For these results, Sobol' indices are only shown in the attached region, and the full flow field is not shown here. The upper and lower uncertainty bounds for $\rho_\infty$, $U_\infty$, $T_\infty$ and $T_{v_\infty}$ were ±10%, with the exception of -20% for $\rho_\infty$. These ranges were selected because this was an initial step in preparation for Bayesian calibration, in order to see what ranges of uncertainties would bracket the experimental observations. The calibration results are discussed in our companion paper [2].**

**Fig. 10    Global sensitivities of the heat flux for Case 1 and Case 4 due to perturbation of freestream conditions. Sensitivities for $\rho_\infty$, $U_\infty$, and $T_\infty$ are shown at the probe locations over the entire flowfield. Sobol' indices were calculated in conjunction with an uncertainty propagation ensemble created using 7%, 3%, and 3% uncertainty on $\rho_\infty$, $U_\infty$, and $T_\infty$, per CUBRC-supplied uncertainty on freestream conditions. In this example, we assume thermal equilibrium in the freestream and set $T_{v_\infty} = T_\infty$, so that $T_{v_\infty}$ is perturbed along with $T_\infty$. Ensemble of 10,000 evaluations of a PCE surrogate (level 2) built from 31 original SPARC runs. SPARC simulations used a $1024 \times 512$ mesh; 100,000 iterations; and a 5-species, 2-temperature model.**
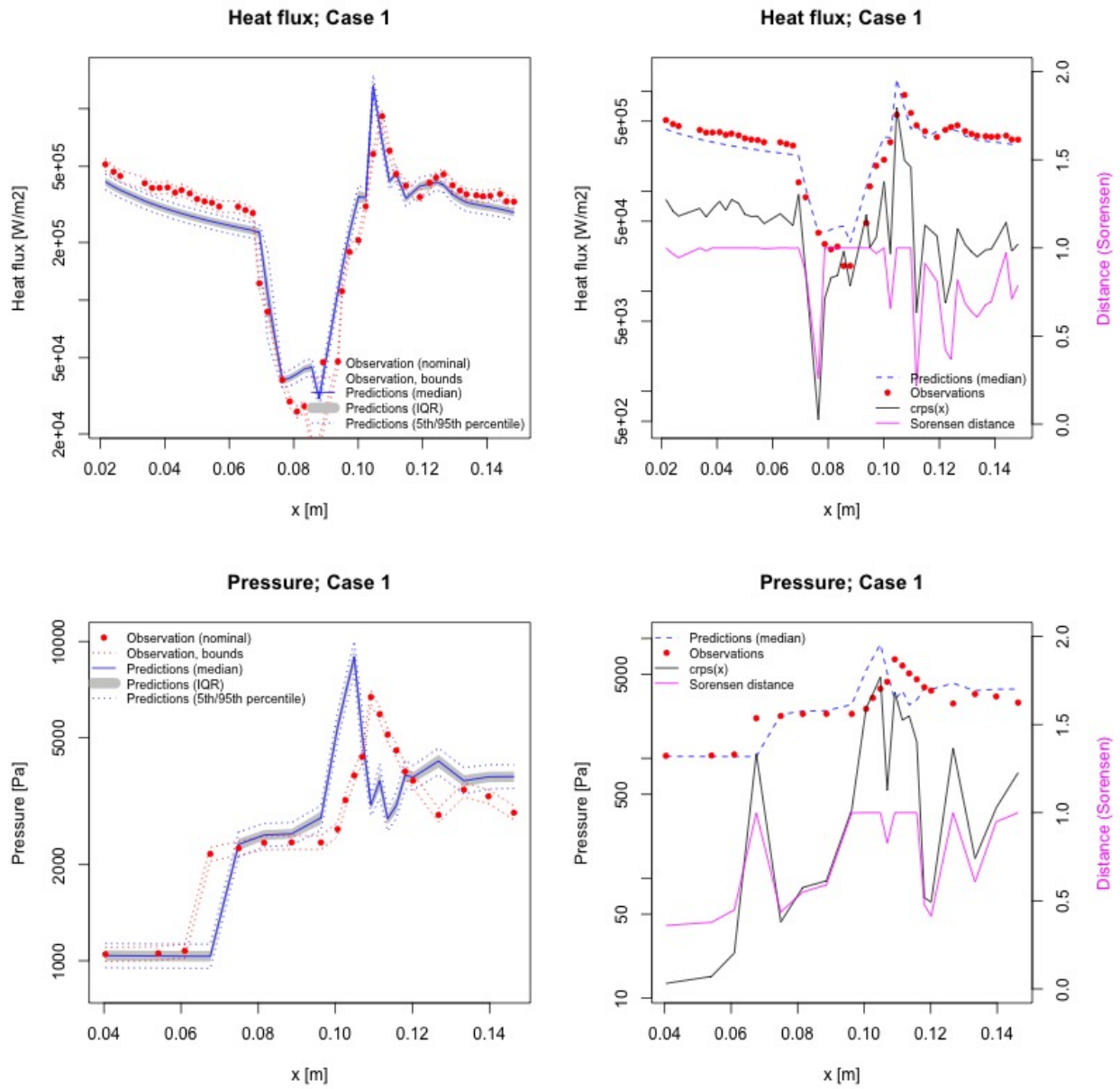
**Fig. 11  Case 1 validation metrics:  CRPS and Sorensen distance using uncertainty propagation results obtained from CUBRC-provided uncertainties for $\rho_\infty$, $U_\infty$, and $T_\infty$.**
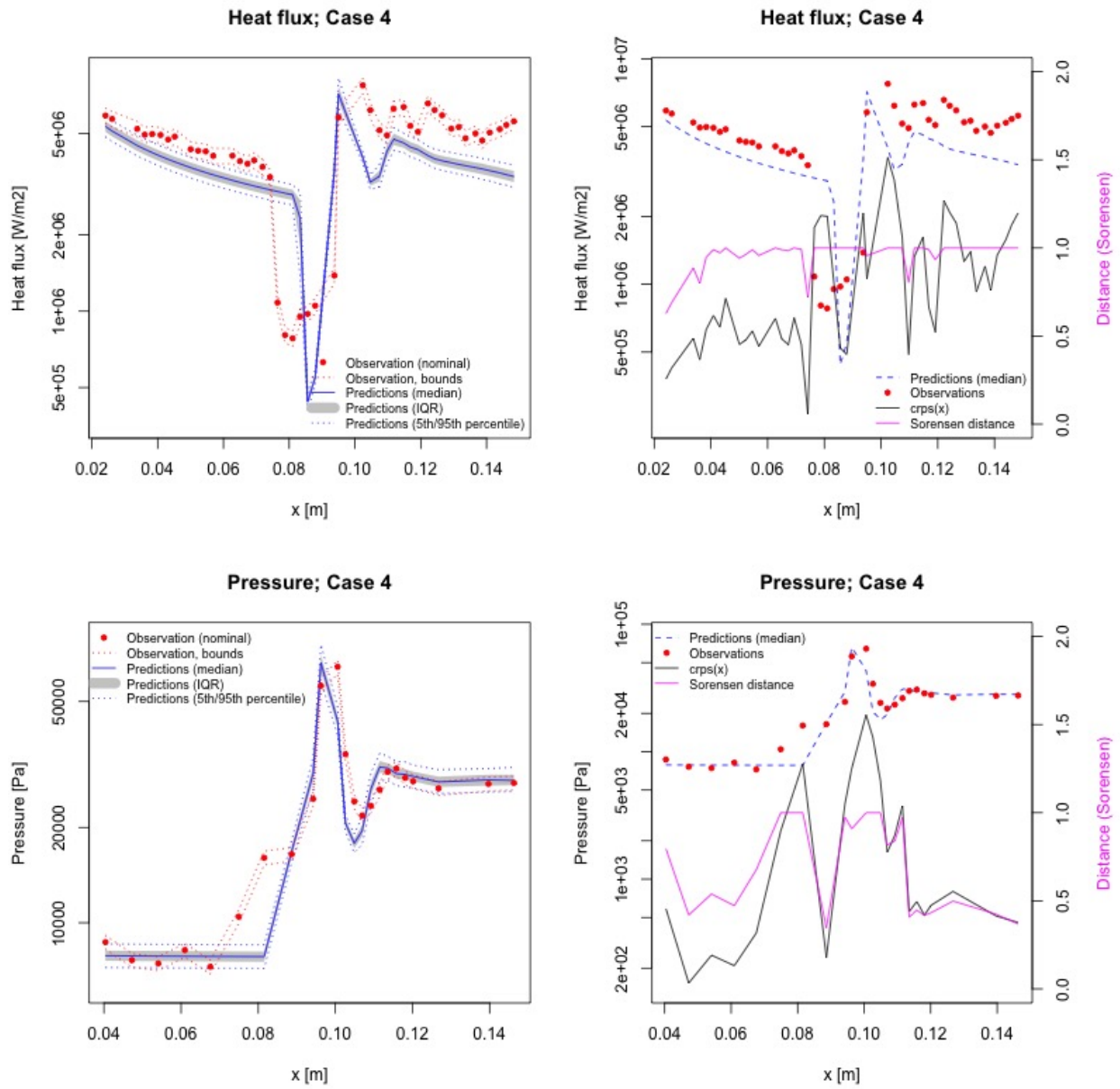
**Fig. 12   Case 4 validation metrics:  CRPS and Sorensen distance using uncertainty propagation results obtained from CUBRC-provided uncertainties for $\rho_\infty$, $U_\infty$, and $T_\infty$.**

From this figure, we see that, at the detachment point at the start of the separation bubble, the numerical errors become very prevalent for the heat flux. At the other locations along the cone, the parametric uncertainty (arising from uncertainty in the freestream conditions) is the dominant source of uncertainty and has the most impact on the difference between the experiment and simulation. The uncertainty comparison for pressure reflects a lower relative bias than for heat flux, as shown in plots in the previous sections. In addition, the numerical and iterative errors are highest near the impingement location for pressure, rather than the separation point for heat flux.

These results show that, if we want to reduce the overall uncertainty, then we need to know more about the freestream conditions. The second priority would be to improve our knowledge of the experimental uncertainty in heat flux and pressure measurements. Improving iterative error would have little improvement overall, and numerical mesh refinement would only make improvements in the separation region. This also reinforces the conclusion that differences in predictions in the separation bubble are still sensitive to further mesh refinement.

Figure 14 shows similar results for Case 1. Comparing Figs. 14 and 13, we see that, in general, across the length of the double-cone, the uncertainties and bias are less for the lower-enthalpy Case 1.

*3. ASME V&V 20 Validation Metric*

The second and third rows of plots in Figures 13 and 14 depict the V&V20 validation metrics described in the Approach section of this paper. The second row shows the absolute bias $|E|$, bracketed by the overall uncertainty, $u_{\text{val}}$. The overall uncertainty bands for pressure are smaller than for the broader uncertainties observed in heat flux. The third row shows the ratio of the absolute bias to the overall uncertainty. A value of $\frac{|E|}{u_{\text{val}}} < 1$ represents an uncertainty greater than the bias, whereas a value greater than one represents uncertainty less than the bias. These plots show that, for heat flux, the ratio is greater than one over most of the cone, except in the laminar, attached region, and, for Case 1, in the aft-cone region. In other words, the bias is larger than the uncertainty in those regions. For Case 1 in the aft-cone region, the ratio is less than one and thus the bias is smaller than the uncertainty. However, for pressure, the ratio is less than one at most locations, except at the singularities that occur at the detachment and directly after the impingement location.

# IV. Conclusions

This paper described our approach and results for uncertainty quantification, sensitivity analysis, and validation assessments. Two previously published studies have shown simulations that under-predict the experimental heat flux measurements in the laminar, attached region on the fore-cone when using the CUBRC-provided freestream conditions [5, 6] for LENS-XX. The validation study described in this paper described our similar results using SPARC. The results for LENS-XX Case 1 and Case 4 indicate that we are unable to bracket the experimental observations of heat flux in the attached region even when considering the ensemble of simulations predicted by a large sampling of perturbed freestream conditions. These results were obtained from an ensemble of uncertainty propagation simulations that perturbed the freestream conditions using CUBRC-provided estimates of uncertainty for $\rho_\infty$, $U_\infty$ and $T_\infty$: $\pm 7\%$, $\pm 3\%$, and $\pm 3\%$. However, when we used a $\pm 15\%$ perturbation, we did bracket the experimental data on the fore-cone.

In this chapter, we presented validation results for Cases 1 and 4 using a refined mesh, with uncertainty propagation computed over the entire flowfield. We also compared uncertainties: parametric, experimental, and numerical (i.e., convergence and iterative). We presented and compared quantitative validation metrics. The results showed that if we want to reduce the overall uncertainty of simulation predictions, then we need to know more information about the freestream conditions. Validation metrics indicated the regions where the uncertainty is greater than the bias between experiments and simulations; these regions include the fore-cone for both Case 1 and 4, and the aft-cone of Case 1.

Here, we introduce potential reasons that numerical simulations cannot predict the experimental observations of LENS-XX studies, particularly in the laminar, attached region of the fore-cone. Our companion paper [2] will use a probabilistic framework and Bayesian inference to further explore these possible causes of the lack of predictive accuracy:

1) *Possible Cause 1*: The freestream conditions may be mis-specified. The true freestream conditions may be outside the measurement error bounds in Table 2. Given our ability to bracket Case 1 and 4 experimental data with a $\pm 15\%$ perturbation of the freestream conditions, our companion paper [2] tests the hypothesis that a mis-specification of the freestream, might be the underlying reason for the lack of predictive accuracy of the CFD simulations.
2) *Possible Cause 2*: The freestream may have spatial variations i.e., it is not radially uniform, and an assumption of axisymmetry (which we, along with all previous studies, have used) may not be warranted.
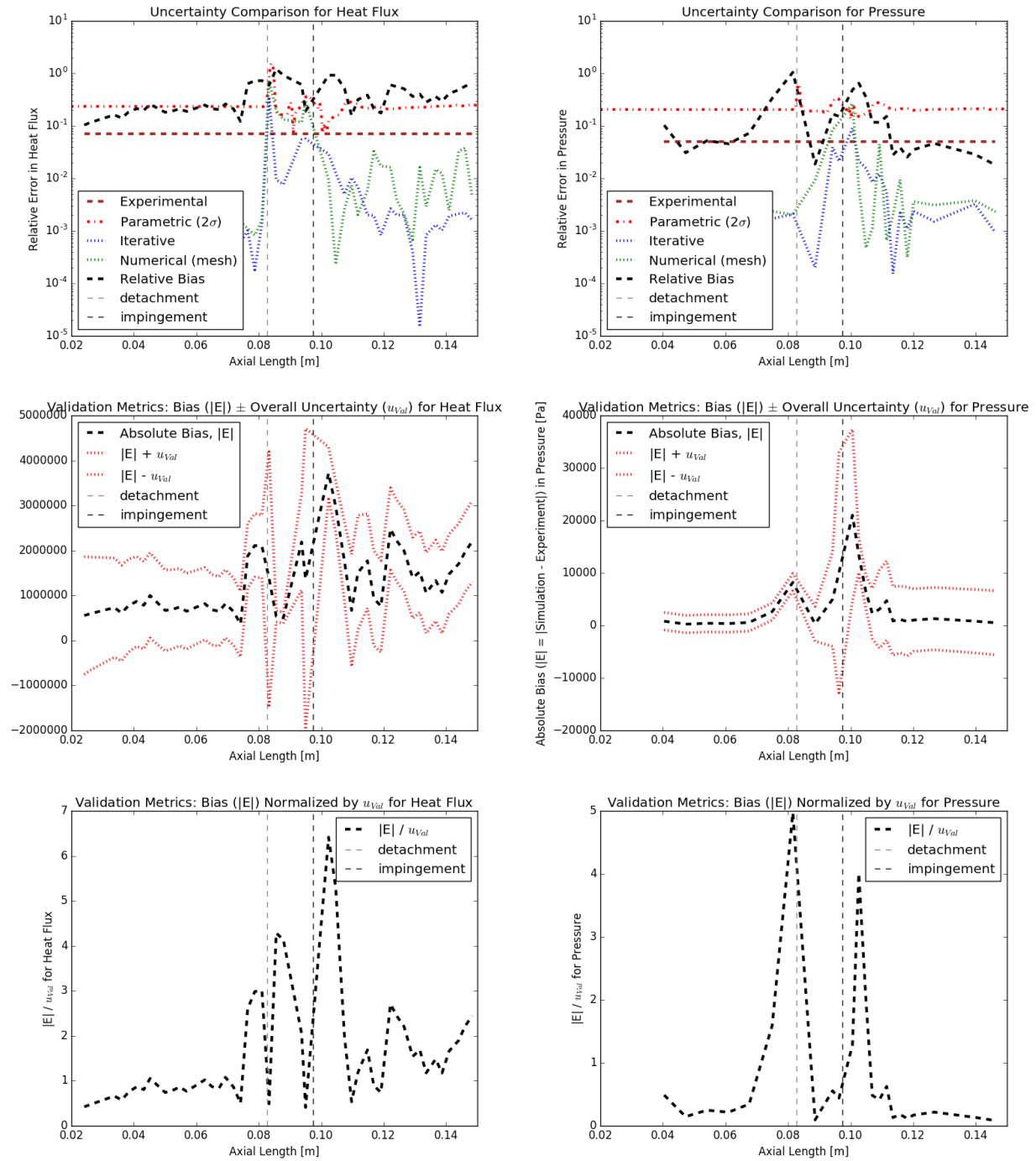
**Fig. 13    Uncertainty comparison and validation metrics for LENS-XX Case 4 using results from the uncertainty propagation studies in this paper and the solution verification studies described in our companion paper [1].**
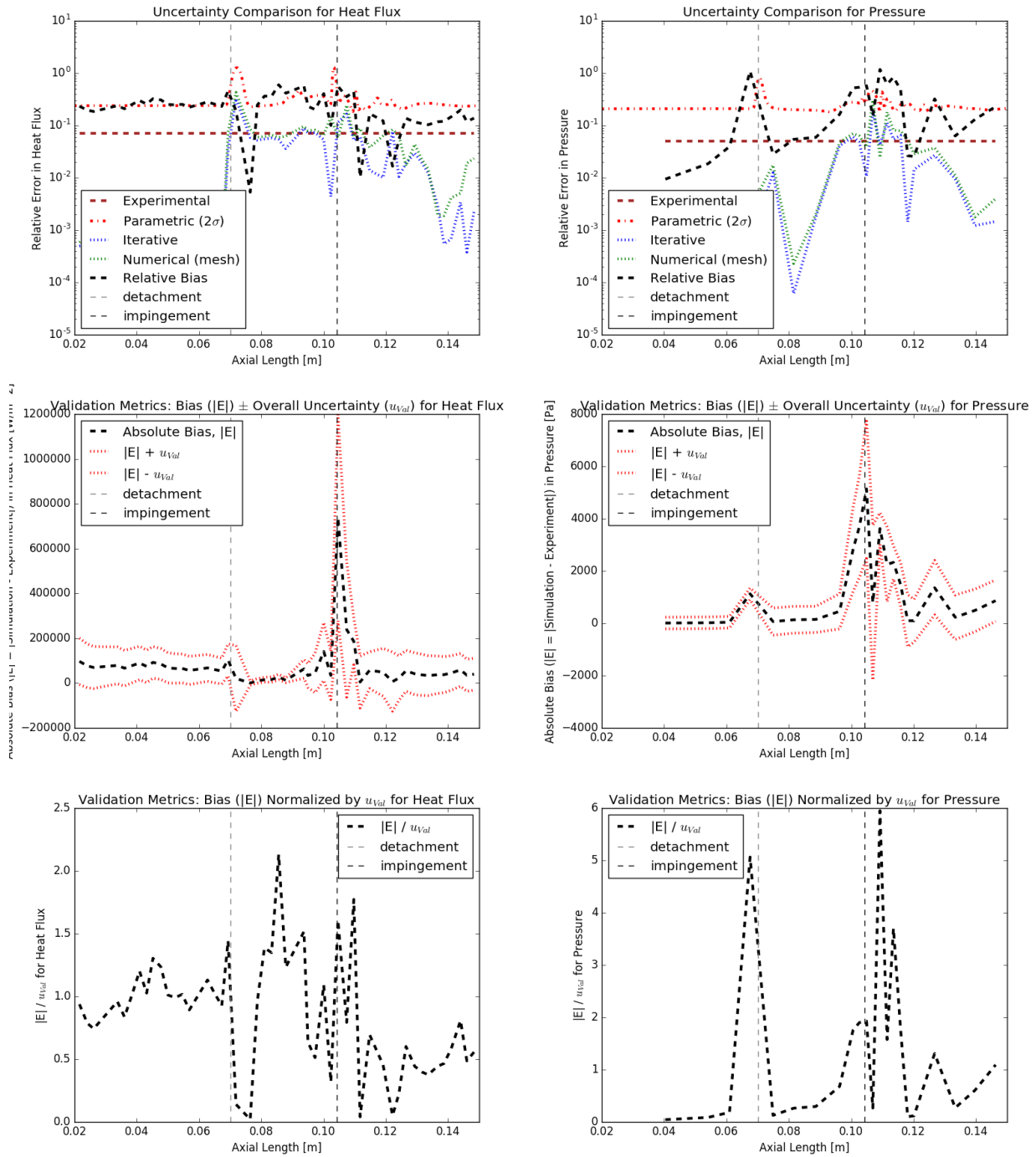
**Fig. 14    Uncertainty comparison and validation metrics for LENS-XX Case 1 using results from the uncertainty propagation studies in this paper and the solution verification studies described in our companion paper [1].**

3) *Possible Cause 3*: The sub-models included in SPARC, e.g., chemical mechanisms, transport properties, etc., are deficient.

Finally, this paper emphasizes the importance of careful measurement of experimental conditions and uncertainty quantification in validation experiments. In combination with our companion papers [1, 2], these results also demonstrate a process of verification, sensitivity analysis, UQ, and quantitative validation assessments for building and assessing credibility of computational simulations.

## Acknowledgments

## References

[1] Carnes, B., Weirs, V. G., Smith, T., and Dinzl, D., "Code verification and numerical error estimation with application to model validation of laminar, hypersonic flow over a double cone," *AIAA 2019 Aerosciences Conference, AIAA SciTech 2019 (AIAA-2019-ABCD)*, 2019.

[2] Ray, J., Kieweg, S., Dinzl, D., Carnes, B., Weirs, V. G., Freno, B., Dinzl, D., Howard, M., Smith, T., Nompelis, I., and Candler, G., "Estimation of Inflow Uncertainties in Laminar Hypersonic Double-Cone Experiments," *AIAA 2019 Aerosciences Conference, AIAA SciTech 2019 (AIAA-2019-ABCD)*, 2019.

[3] ASME V&V 10-2006, *Guide for Verification and Validation in Computational Solid Mechanics*, ASME, New York, NY, 2006.

[4] MacLean, M., Holden, M. S., and Dufrene, A., "Measurements of Real Gas Effects on Regions of Laminar Shock Wave/Boundary Layer Interaction in Hypervelocity Flows," Tech. rep., CUBRC Inc., 2014. `https://www.cubrc.org/_iassets/docs/laminar-xx-paper.pdf`.

[5] Youssefi, M. R., and Knight, D., "Assessment of CFD capability for hypersonic shock wave laminar boundary layer interactions," *Aerospace*, Vol. 4, No. 25, 2017. doi:10.3390/aerospace4020025.

[6] Hao, J. A., Wang, J. Y., and Lee, C. H., "Numerical Simulation of High-Enthalpy Double-Cone Flows," *AIAA Journal*, Vol. 55, No. 7, 2017, pp. 2471–2475. doi:10.2514/1.j055746.

[7] Candler, G. V., "Next-Generation CFD for Hypersonic and Aerothermal Flows (Invited)," *22nd AIAA Computational Fluid Dynamics Conference, AIAA AVIATION Forum, (AIAA 2015-3048)*, 2015. doi:10.2514/6.2015-3048.

[8] Park, C., "On convergence of computation of chemically reacting flows," *23rd AIAA Aerospace Sciences Meeting (AIAA-1985-0247)*, 1985. doi:10.2514/6.1985-247.

[9] Marrone, P. V., and Treanor, C. E., "Chemical relaxation with preferential dissociation from excited vibrational levels," *Physics of Fluids*, Vol. 6, No. 9, 1963, pp. 1215–1221.

[10] Holden, M., "Experimental studies of laminar separated flows induced by shock wave/boundary layer and shock/shock interaction in hypersonic flows for CFD validation," *38th Aerospace Sciences Meeting and Exhibit, Aerospace Sciences Meetings, (AIAA-2000-0930)*, 2000. doi:10.2514/6.2000-930.

[11] Harvey, J. K., Holden, M. S., and P., W. T., "Code Validation Study of Laminar Shock/Boundary Layer and Shock/Shock Interactions in Hypersonic Flow. Part B: Comparison with Navier–Stokes and DSMC Solutions," *AIAA Paper 2001-1031B*, 2001.

[12] Nompelis, I., Candler, G. V., and Holden, M. S., "Effect of vibrational nonequilibrium on hypersonic double-cone experiments," *AIAA Journal*, Vol. 41, No. 11, 2003, pp. 2162–2169. doi:10.2514/2.6834.

[13] Nompelis, I., Candler, G. V., MacLean, M., Wadhams, T., and Holden, M., "Numerical Investigation of High Enthalpy Chemistry on Hypersonic Double-Cone Experiments," *43rd Aerospace Science Meeting and Exhibit (AIAA Paper 2005-0584)*, 2005.

[14] Smith, R. C., *Uncertainty quantification: Theory, implementation and applications*, Society for Industrial and Applied Mathematics, Computational Science and Engineering Series, 2014.

[15] Adams, B., Bauman, L., Bohnhoff, W., Dalbey, K., Ebeida, M., Eddy, J., Eldred, M., Hough, P., Hu, K., Jakeman, J., Stephens, J., Swiler, L., Vigil, D., , and Wildey, T., "Dakota, A Multilevel Parallel Object-Oriented Framework for Design Optimization, Parameter Estimation, Uncertainty Quantification, and Sensitivity Analysis: Version 6.0 User's Manual," Tech. Rep. Technical Report SAND2014-4633, Sandia National Laboratories, Albuquerque, NM, July 2014. Updated November 2015 (Version 6.3).

[16] Vincenti, W., and Kruger, C., *Introduction to physical gas dynamics*, Krieger Publishing Company, Malabar, FL, USA, 1965.

[17] Millikan, R., and White, D., "Systematics of vibrational relaxation," *Journal of Chemical Physics*, Vol. 39, 1963, pp. 3209–3213.

[18] Park, C., "Review of chemical-kinetic problems of future NASA missions I: Earth entries," *Journal of Thermophysics and Heat Transfer*, Vol. 7, No. 3, 1993, pp. 385–398. doi:10.2514/3.431.

[19] Blottner, F. G., Johnson, M., and Ellis, M., "Chemically reacting viscous flow program for multicomponent gas mixtures," Tech. Rep. Technical Report SC-RR-70-754, Sandia National Laboratories, Albuquerque, NM, 1971.

[20] Anderson, J. D., *Hypersonic and High-Temperature Gas Dynamics, Second Edition*, AIAA Education Series, 2006. doi: 10.2514/4.861956.

[21] Holden, M. S., and P., W. T., "Code Validation Study of Laminar Shock/Boundary Layer and Shock/Shock Interactions in Hypersonic Flow. Part A: Experimental Measurements," *AIAA Paper 2001-1031A*, 2001.

[22] Druguet, M. C., Candler, G. V., and Nompelis, I., "Effect of numerics on Navier–Stokes computations of hypersonic double-cone flows," *AIAA Journal*, Vol. 43, No. 3, 2005, pp. 616–623. doi:10.2514/1.6190.

[23] Phipps, E. T., and Gay, D. M., "Sacado Automatic Differentiation Package," `http://trilinos.org/packages/sacado/`, 2016.

[24] Bartlett, R. A., Gay, D. M., and Phipps, E. T., "Automatic Differentiation of C++ Codes for Large-Scale Scientific Computing," *Computational Science – ICCS 2006*, Lecture Notes in Computer Science, Vol. 3994, edited by V. N. Alexandrov, G. D. van Albada, P. M. A. Sloot, and J. Dongarra, Springer, Heidelberg, 2006, pp. 525–532. doi:10.1007/11758549_73.

[25] Phipps, E. T., Bartlett, R. A., Gay, D. M., and Hoekstra, R. J., "Large-Scale Transient Sensitivity Analysis of a Radiation-Damaged Bipolar Junction Transistor via Automatic Differentiation," *Advances in Automatic Differentiation*, edited by C. H. Bischof, H. M. Bücker, P. D. Hovland, U. Naumann, and J. Utke, Springer, 2008, pp. 351–362. doi:10.1007/978-3-540-68942-3_31.

[26] Phipps, E. T., and Pawlowski, R. P., "Efficient Expression Templates for Operator Overloading-based Automatic Differentiation," *Recent Advances in Algorithmic Differentiation*, edited by S. Forth, P. Hovland, E. Phipps, J. Utke, and A. Walther, Springer, 2012.

[27] Gneiting, T., and Raftery, A. E., "Strictly Proper Scoring Rules, Prediction, and Estimation," *Journal of the American Statistical Association*, Vol. 102, No. 477, 2007, pp. 359–378. doi:10.1198/016214506000001437, URL `http://pubs.amstat.org/doi/abs/10.1198/016214506000001437`.

[28] Gneiting, T., Balabdaoui, F., and Raftery, A. E., "Probabilistic forecasts, calibration and sharpness," *Journal of the Royal Statistical Society: Series B (Statistical Methodology)*, Vol. 69, No. 2, 2007, pp. 243–268. doi:10.1111/j.1467-9868.2007.00587.x, URL `http://dx.doi.org/10.1111/j.1467-9868.2007.00587.x`.

[29] Cha, S.-H., "Comprehensive survey on distance/similarity measures between probability density functions," *International Journal of Mathematical Models and Methods in Applied Sciences*, Vol. 1, No. 4, 2007.

[30] ASME V&V 20-2009, *Standard for Verification and Validation in Computational Fluid Dynamics and Heat Transfer*, ASME, New York, NY, 2009.

[31] Candler, G., Johnson, H., Nompelis, I., Gidzak, V., Subbareddy, P., and Barnhardt, M., "Development of the US3D Code for Advanced Compressible and Reacting Flow Simulations," *AIAA Paper 2015-1893*, 2015.